Effects of particle collection in a premixed stagnation flame synthesis with a rotating substrate

Manoel Yohanes Manuputty [1,2], Rong Xu [1,2], Markus Kraft [1,2,3,4]

released: January 31, 2022

[1] School of Chemical
and Biomedical Engineering
Nanyang Technological University
62 Nanyang Drive
Singapore, 637459

[2] CARES
Cambridge Centre for Advanced
Research and Education in Singapore
1 Create Way
CREATE Tower, #05-05
Singapore, 138602

[3] Department of Chemical Engineering
and Biotechnology
University of Cambridge
Philippa Fawcett Drive
Cambridge, CB3 0AS
United Kingdom

[4] The Alan Turing Institute
London
United Kingdom

UNIVERSITY OF
CAMBRIDGE

Abstract

A rotating stagnation plate is widely used as a substrate and to provide a cooling mechanism in a premixed stagnation flame synthesis. The collection of particles from the rotating plate could be done in two ways: the conventional interval particle collection (IPC) method and a continuous particle collection (CPC). The CPC approach was achieved by a simple modification to the rotating plate to minimise further exposure of the deposited particles to the flame during synthesis. The effects of the deposition time and the rotation speed on the properties of titanium dioxide (TiO_2) particles are investigated experimentally. A two-cycle thermogravimetric analysis and mass spectrometry is proposed as a simple way to quantify the amounts of the oxygen vacancy (OV) and the organic component (OC) in TiO_2 particles. Further, powder X-ray diffraction (XRD) analysis is used to determine the crystallinity and phase composition of the prepared samples. For IPC, it was found that the properties of the collected samples are dependent on the deposition time. This creates an undesirable correlation between properties and synthesis yield. On the other hand, CPC approach allows for a continuous synthesis in which the particle properties are invariant with respect to the synthesis yield. The tunability of the particle properties is still achievable by controlling the rotation speed in the CPC. The CPC method thus provides a practical way to prepare flame-synthesised metal oxide nanoparticles for applications that require a large amount of samples such as catalysis.
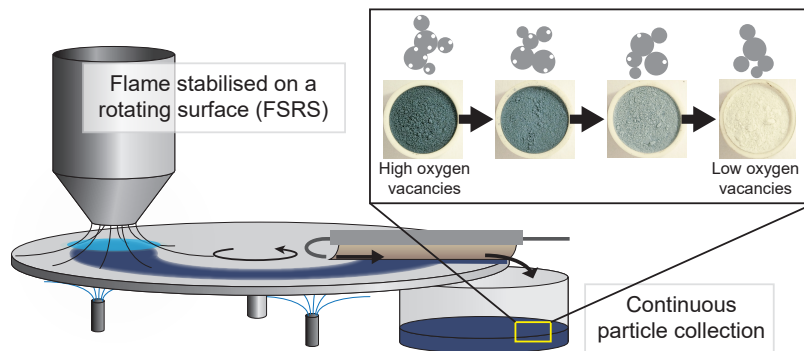
Highlights

- Continuous collection method is introduced for stagnation flame synthesis
- Continuous and interval collection methods are evaluated systematically
- Oxygen vacancies and crystallinity are used to assess the collection effects
- Continuous method allows for a longer operation while preserving particle properties

1

Contents

1 Introduction

Stagnation flames have been widely used for fundamental combustion studies due to the simple geometry and the low-dimensional flow field [15]. The divergence stabilised stagnation flames (DSSFs), in particular, have been used to study the formation of metal oxide nanoparticles, including gas-phase mechanisms, gas-to-particle transition, and particle growth dynamics [2, 6, 10].

Wang and coworkers first demonstrated the concept of the flame stabilised on a rotating surface (FSRS) configuration to prepare TiO_2 thin films for dye sensitised solar cells (DSSCs) and gas sensors [19–21]. The rotation of the stagnation surface cools the substrates and minimise further particle growth/sintering once the particles are collected. The high temperature and short residence time typical in DSSFs result in the formation of highly crystalline nanoparticles with small (<15 nm) and uniform size distributions. The crystal phase composition was shown to be tunable by controlling the flame equivalence ratio [9]. More recent studies also demonstrated that the short residence time facilitated the formation of metastable phases and oxygen deficient TiO_2 [11, 13].

The unique properties of the DSSF-made metal oxides make them candidates to be explored for catalysis [22]. For example, the surface oxygen vacancies of TiO_2 has been shown to affect the strong metal-support interaction (SMSI) when used as a catalyst support [4, 7]. Thus, the ability to tune the amount of oxygen vacancies is important. For TiO_2, this is often associated qualitatively with the blue coloration of the powder [1, 18]. However, systematic studies on the effects of flame conditions on oxygen vacancies in TiO_2 are lacking. This is likely because the quantitative analysis of the oxygen vacancy is challenging [14].

A low synthesis yield has been one of the challenges with laboratory-scale DSSF synthesis, often making it impractical for applications requiring a relatively large amount of samples. This is partly due to the non-complete conversion of precursor to particle as a result of the short residence time in the flame.

In addition, a short deposition time is often required in order to obtain particles with certain desired properties. The proximity of the stagnation surface to the flame in DSSFs means that the deposited particles are continually exposed to a high temperature, resulting in further transformations. This leads to non-uniform distributions of particles collected on the stagnation surface. While the effects of the stagnation temperature on the flame structure and the particle growth dynamics have been investigated before [5, 10], its effects on post-deposition particle growth/transformation are often assumed to be negligible.

Theoretically, this undesirable effect is minimised in FSRS by convective cooling of the stagnation surface through the plate rotation. Additional cooling mechanism such as using gas jets on the opposite side of the rotating plate is often employed [19]. However, the effects of the cooling mechanisms and the deposition time on the particle properties have not been studied systematically. For example, oxygen vacancies in TiO_2 is easily oxidised during the deposition using the FSRS. This is qualitatively shown by the color change from dark blue to white as deposition time increases in our previous work [23]. The formation of some metastable phases also require a very short residence time in order to minimise further exposure to the flame [11]. In order to achieve this, the flame has to be

stopped periodically to collect the particles from the rotating surface, effectively running it as a batch reactor.

The purpose of this paper is to demonstrate the concept of a continuous particle collection (CPC) approach to improve the synthesis yield, reproducibility, and tunability of the stagnation flame synthesis with a rotating substrate. This is in contrast to the interval particle collection (IPC) approach conventionally used with such a system. The effects of the collection approach and the key operating parameters are assessed using a two-cycle TGA-MS method. The method provides a simple way to estimate the amounts of the oxygen vacancy and the organic component in the products. Further, a simple peak fitting of the powder XRD data is used to assess the phase composition and the crystallinity.

2 Experimental methods

2.1 Flame synthesis

The stagnation flame synthesis system used in this work is similar to those reported elsewhere [13, 19, 20]. A premixed mixture is issued from a downward facing aerodynamic nozzle with a total volumetric flow rate of 28 slpm. The mixture consists of 6% C_2H_4, 15% O_2, and 79% Ar, which corresponds to an equivalence ratio (ϕ) of 1.2. The nozzle has an exit diameter of 14 mm, resulting in an exit velocity of 436 cm/s at 150°C. The premixed jet from the nozzle impinges on a stagnation surface located at 10 mm from the nozzle. Upon ignition, a stable flat flame is formed, approximately 3 mm above the stagnation surface. Titanium tetraisopropoxide (TTIP, $\geq$ 97%, Sigma-Aldrich) is injected into the unburned gas mixture with a syringe pump at 20 ml/h, corresponding to 900 ppm Ti mole fraction. The gas line, precursor line, and burner surface are heated to 150°C to prevent TTIP condensation. In order to ensure thermal equilibrium of the stagnation surface, the undoped flame is first run for 10 minutes before TTIP is injected. A shroud flow of 20 slpm N_2 gas is used to stabilise and shield the jet flow from the ambient air.

The stagnation surface consists of a stainless steel disk with 300 mm diameter and 6 mm thickness. The disk is attached to a motorised rotary stage (X-RSB060AD, Zaber Technologies Inc.). The rotation axis is located at 100 mm from the burner centerline. During the synthesis, the disk acts as a deposition substrate. The rotation provides some convective cooling of the deposited TiO_2 to prevent further sintering or oxidation. It is further cooled by four compressed dry air (CDA) jets placed under the plate with a total flowrate of 100 lpm.

2.2 Particle collection

Two approaches for particle collection are employed. These are illustrated in Fig. 1. The first is termed the *interval particle collection (IPC)* method, shown in Fig. 1(a). In this method, the deposition is done over a specific period of time after which the experiment is stopped, *i.e.* flame extinguished, and the deposited particles collected from the rotating disk. In order to maximise the convective cooling, the rotating disk is usually operated at
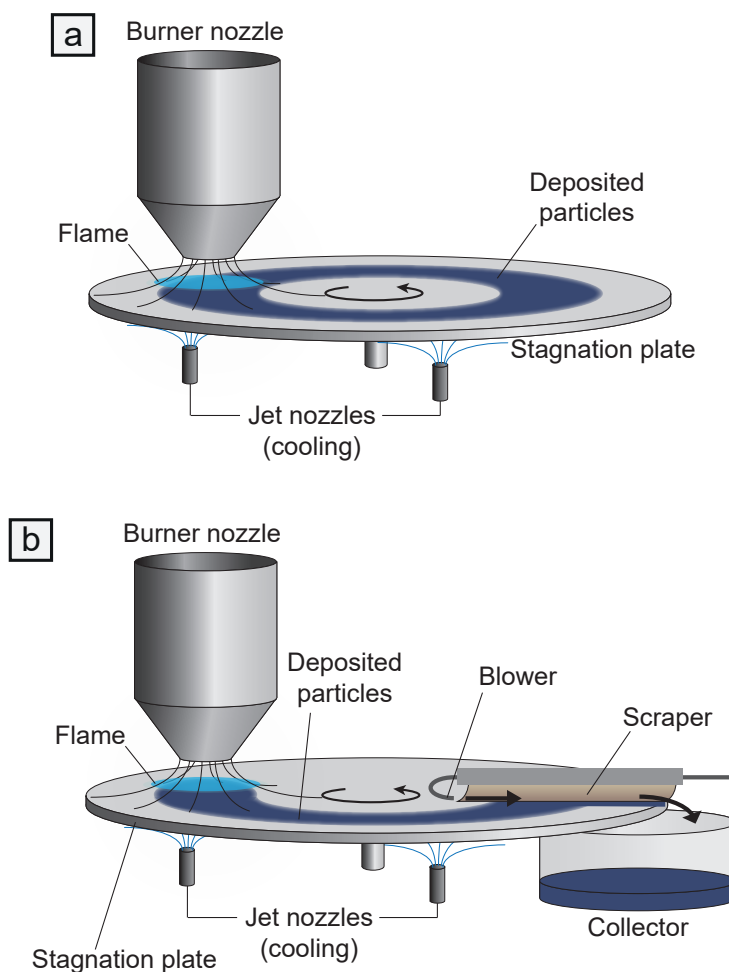
Figure 1: *Schematics of the flame synthesis setup with (a) interval particle collection (IPC) and (b) continuous particle collection (CPC) approaches.*

a very high rotation speed, typically 100–300 rpm. Assuming the deposition area under the flame is 40 mm in diameter, this corresponds to approximately 10–50 ms of flame exposure per revolution. For a 5 minute deposition, this translates to approximately 19 s of total flame exposure (the total time in which any deposition area passes through the flame).

The second method is termed the *continuous particle collection (CPC)* method. This is achieved by the addition of a scraper placed on the opposite side of the rotating disk as shown in Fig. 1(b). The scraper is made of a flexible heat resistant sheet (0.25 mm thickness, Nomex®, DuPont). The scraper continuously scrapes the freshly deposited TiO_2 which is then blown to the side and collected in a collector. The blower, made of a 1/8 in stainless steel tube, delivers a small flow of CDA (3.5 slpm) to cool and blow the samples. In this method, the scraper introduces a significant off-centered load to the motor which limits the maximum rotation speed achievable. In this case, a rotation speed of 0.1–1 rpm is used in this work for CPC. This corresponds to approximately 4–40 s of flame exposure per evolution.

The samples discussed in this paper are labelled according to the collection approach, plate rotation speed, and the deposition time used during the synthesis. For example, 'CPC-1rpm-30min' refers to the sample collected with the CPC method, using 1 rpm plate rotation speed and 30 min deposition time.

2.3 Material characterisations

The thermal gravimetric analysis is performed with a thermobalance (TGA/DSC 2, Mettler Toledo). For each analysis, 40–50 mg of sample is used directly after synthesis. The sample is compacted with a mortar and pestle as the collected powder was very light and difficult to handle. A mass spectrometer (Hiden QGA, Hiden Analytical) is used to monitor the CO_2 concentration in the TGA effluent gases.

In order to elucidate the physical processes taking place during the heating, the weight loss and the CO_2 signal are monitored over a wide temperature range up to 800°C for a selected sample. The sample is first flushed at 40°C with 50 ml/min N_2 for 30 min and then 50 ml/min synthetic air for 60 min. Subsequently, the sample is heated to 800°C at 5°C/min and then held for 30 min, followed by cooling to 40°C at -20°C/min under 50 ml/min N_2.

For oxygen vacancy (OV) and organic component (OC) analysis, the weight loss and CO_2 signal are monitored over two heating/cooling cycles. In between the cycles, the sample is exposed to ambient air for 30 min to allow water readsorption. Each cycle consists of five heating stages (A–E) over a temperature range of 40–400°C. The samples are first heated to 120°C at 10°C/min under 50 ml/min N_2 and held at this temperature for 30 min (stage A). The method gas is then switched to 50 ml/min synthetic air for another 60 min to remove the physically adsorbed water (stage B). The samples are subsequently heated to 200°C at 5°C/min and held for 120 min (stage C). This is followed by further heating to 400°C at 5°C/min and 30 min isotherm (stage D). Finally, the samples are cooled to room temperature at -20°C/min under 50 ml/min N_2 (stage E).

Electron paramagnetic resonance (EPR) spectra are obtained with a JES FA200 spectrometer (JEOL) operating at X-band frequency (8-10 GHz). The EPR spectra were recorded using 100 kHz modulation frequency, 0.6 mT modulation amplitude, 0.03 s time constant, 4 min sweep time, at temperature of 123 K.

Powder X-ray diffraction (XRD) patterns of the collected samples are recorded with a D8 Advance diffractometer (Bruker) with Cu K_α radiation (40 kV, 30 mA). The 2θ scan range is 10–80° with a step size of 0.03° and 0.7 s per step. Zero-background silicon sample holders with 0.1 mm cavities are used. The peak fitting is performed using TOPAS Academic (version 6) [3].

TEM images are obtained with a JEOL JEM-2100F operating at 200 keV. The particle size distributions are measured manually from the TEM images with a MATLAB script used in our previous work [12].

3 Results and discussion

3.1 Oxygen vacancy and organic component

During the temperature ramp, three main physical processes affecting the sample weight are expected to occur. These are (1) water desorption, (2) carbon oxidation, and (3) OV oxidation. The first and second result in a weight loss while the third results in a weight gain.

Figure 2(a) shows the TGA-MS results for a wide temperature scan up to 800°C. The derivative plot shows two main negative peaks (weight loss) in 50–150 and 250–400°C ranges. The first weight loss is associated with desorption of physically adsorbed water which is consistent with other reports in the literature [17]. The second weight loss peak is mainly attributed to the combustion of OC as indicated by the MS signal for CO_2. The OC combustion starts at temperature as low as 150°C and reaches a maximum at 335°C. The MS signal shows three distinguishable peaks which likely correspond to different chemical environments of carbon. In addition, chemically bound water desorption is also expected to contribute to the mass loss up to 600°C. It generally occurs gradually over a wide range of temperature [17]. This can be seen from the slight weight loss in 400–600°C after OC combustion is complete.

No distinguishable weight gain can be inferred from Fig. 2(a) to indicate OV oxidation. However, Fig. 2(b) shows the blue coloration disappears when the sample is held at $T = 200$°C (heating stage C) compared to when the sample is held at $T = 120$°C (heating stage B). Similarly, the qualitative EPR spectra in Fig. 2(c) show marked changes between 120 and 200°C. As prepared and 120°C samples show a strong broad absorption with a g-value of 1.94. This is often attributed to surface Ti^{3+} [16]. As the sample is heated up to 200°C, the broad absorption at g-value of 1.94 disappears and a narrow absorption at g-value of 2.00 is observed, indicating lattice-embedded Ti^{3+}. This coincides with the color change of the sample from dark blue to grey. As the sample is further heated to 400°C, no paramagnetic centres can be observed anymore and the sample turns from grey to white, indicating carbon oxidation which is consistent with the MS signal in Fig. 2(a). Thus, the EPR spectra suggest that OV oxidation mainly occurs between 120–200°C range which overlaps with the other processes described above.

In order to estimate the OV amount, a two-cycle TGA-MS measurement is used. The purpose is to separate the reversible processes (water desorptions, physcial and chemical) and the irreversible processes (OV oxidation and OC combustion). The reversible processes are assumed to occur in both cycles of heating while the irreversible processes occur only in the first cycle. For each cycle, the samples are heated to $T = 120$, 200, and 400°C followed by a period of isotherms. The temperature range is limited to 400°C as it is sufficient to complete the OV oxidation and OC combustion while minimising any microstructural changes such as sintering and phase transformation which are known to occur at higher temperatures.

Figure 3 shows the normalised weights and MS signals monitored during the two-cycle TGA measurement for P25 sample. The sample temperature is shown in Fig. 3(a) with 5 heating stages labelled A–E. The weights of the sample at the different stages are averaged
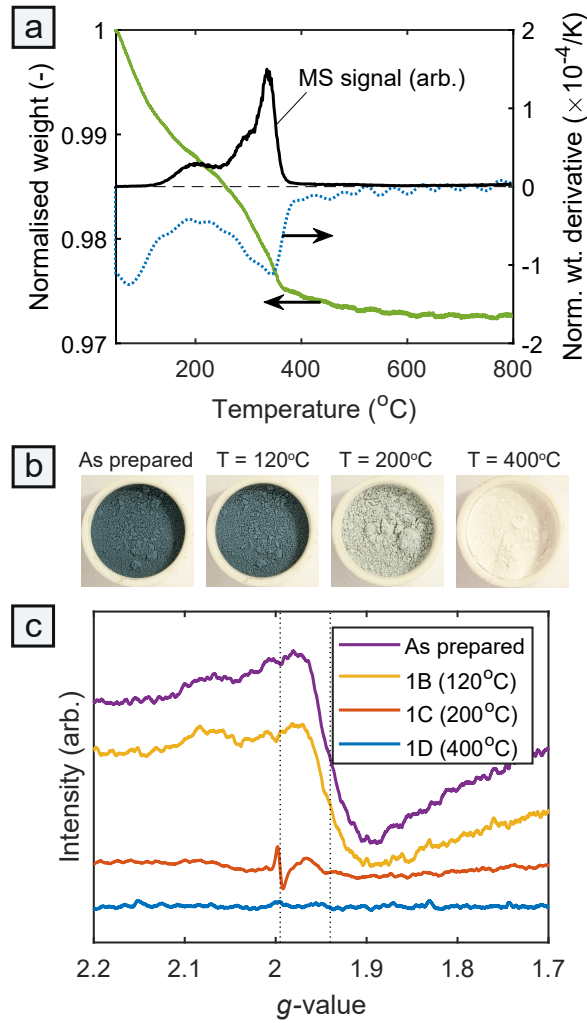
Figure 2: *(a) Normalised weight, its derivative, and the MS signal from wide scan TGA measurement up to 800°C, (b) digital photographs and (c) the qualitative EPR spectra showing the changes in color and the paramagnetic centres during the heating stages (CPC-1rpm-30min sample). The dotted vertical lines denote g-values of 1.94 and 2.00.*

over 24 minute period towards the end of the isotherm part of each stage. The average weights are annotated accordingly in Fig. 3(a) for both cycles, *e.g.*, w_{1B}, w_{2B}, w_{1C}, *etc*. It is noted that the sample weight increases during cooling (stage E) due to the reversible water adsorption.

The MS signals in Fig. 3(b) show that the OC combustion occurs only in the first cycle (irreversible). The CO_2 release is detected in stages C and D. The amount of OC combusted is assumed to be proportional to the cumulative MS signal for each stage, *i.e.* δ_C and δ_D. The ratio of OC combusted in stages C and D is given by R. The step changes in the MS signal between stages A to B and D to E indicate the switch of method gas between N_2 and synthetic air.
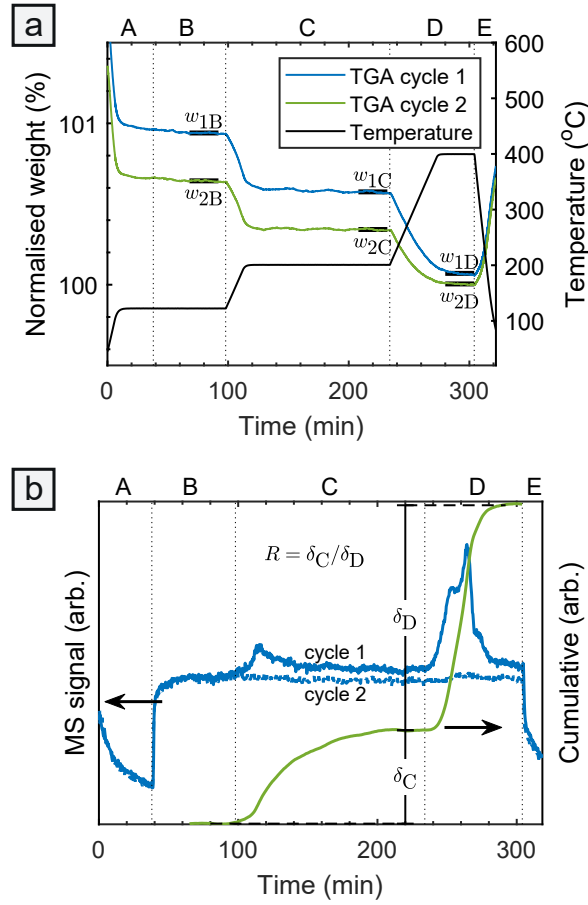
8

Figure 3: *TGA and MS results for P25 during the heating stages denoted by the dotted vertical lines: (a) The temperature and the normalised weights (against w_{2D}). The weights, w, at the different stages are averaged over 24 minute periods denoted by the thick horizontal lines. (b) The MS signals for CO_2 (m/z = 44) and the cumulative signal from the cycle 1 measurement. The cumulative signals in stages C and D are denoted as δ_C and δ_D, respectively.*

Assuming that carbon oxidation is the only irreversible process occuring in stage D, the weight change due to OC oxidation, Δw_C, can be written as

$$\Delta w_C = (R+1)\left[(w_{1C} - w_{2C}) - (w_{1D} - w_{2D})\right]. \tag{1}$$

The weight change due to OV oxidation, Δw_O, can be calculated as folows,

$$\Delta w_O = (w_{1C} - w_{2C}) - (w_{1B} - w_{2B}) + \frac{R}{R+1}\Delta w_C. \tag{2}$$

Subsequently, the OV concentration (the fraction of lattice oxygen replaced with vacancies) is given by

$$OV\ (at.\ \%) = \Delta w_O \frac{M_{TiO_2}}{M_{O_2}}, \tag{3}$$

9

where M_{TiO_2} and M_{O_2} are the molar mass of TiO_2 and O_2, respectively. For the P25 sample, the OV and OC (Δw_C) are determined to be $\sim$0 at.% and $\sim$0.2 wt.%, respectively.

The TGA-MS results and the derived OV and OC amounts are given in Appendix A.3 for all samples used in this work. The effects of the particle collection on the OV and OC are discussed below.

3.2   Deposition time and rotation speed

The effects of the plate rotation speed and the deposition time on the particle properties are investigated for both IPC and CPC methods. The TEM images in Figs. 4(a-b) show mainly spherical particles with some larger particles appear slightly faceted. The particles exhibit a minimal degree of sintering which is consistent with our previous findings [8, 12]. The particle size distributions from TEM image analysis for selected conditions are shown in Fig. 4(c). Additional data is supplied in Appendix A.4. The median particle sizes are between 10–11 nm regardless of the collection method, rotation speed and the deposition time. This suggests that for the conditions considered in this work, the particles are sufficiently cooled such that no significant particle growth/sintering occurs after the deposition. This is not surprising given the estimated plate temperature of $< 200°$C (see Appendix A.1) is well below the sintering temperature of TiO_2.
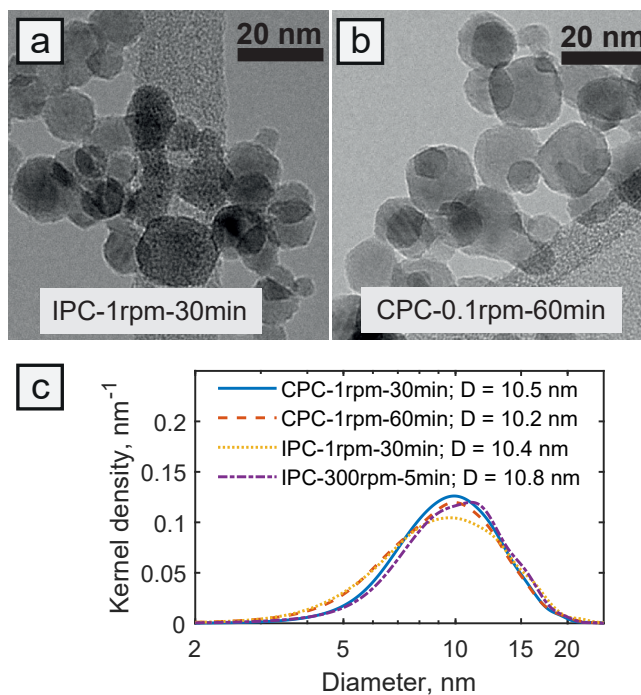

Figure 4: *(a-b) Examples of TEM images, and (c) the measured particle size distributions from TEM size analysis for selected samples. The median particle sizes, D, are included in the legend.*

Figure 5(a) shows the powder XRD data for selected IPC and CPC samples. Anatase,
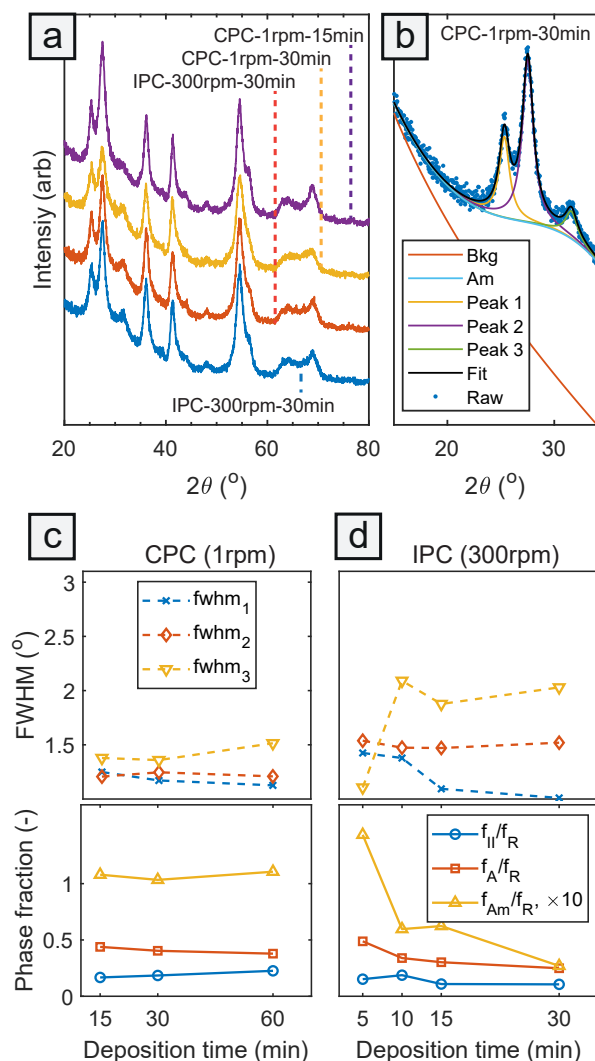
Figure 5: *Powder XRD analysis of selected samples: (a) Measured powder XRD data, (b) an example of the fitted XRD data with 2θ range of 15–34° showing individual components for CPC-1rpm-30min sample, (c-d) the full width at half maximum (fwhm) of the fitted peaks and the estimated phase fractions as a function of deposition time for CPC and IPC methods. Abbreviations – Bkg: background, Am: amorphous, A: anatase, R: rutile, II: TiO_2-II, fwhm: full width at half maximum.*

rutile, and TiO_2-II phases are present as reported previously for flames with equivalence ratio of 1.1–2.0 [11]. A full profile Rietveld refinement was not possible due to significant overlaps and broadening of peaks from rutile, anatase and TiO_2-II. Instead, a simple fitting exercise was performed to quantitatively assess the effects of the collection conditions on the phase composition and crystallinity. The 2θ range of 15–34° was chosen as this range contains the main peaks of all phases, including an amorphous bump, while peak overlaps are minimised. Figure 5(b) shows an example of the deconvoluted peaks from the fitting. Three Lorentzian functions are used to model the peaks at 25.3, 27.3, and 31.6°. The first

peak contains both anatase and TiO_2-II phases while second and third peaks correspond to rutile and TiO_2-II, respectively. A Gaussian function is used to represent the broad peak from the amorphous phase ('Am'). Additional details of the fitting procedure and the refined parameters are supplied in Appendix A.2.

The full width at half maximum (fwhm) of the fitted peaks signifies the crystallinity/crystal size as the size broadening is predominant at small 2θ. A smaller fwhm indicates a larger crystallite size and thus better crystallinity. In addition, the intensities of the peak can be attributed to the individual phases such that the relative fractions of the phases can be estimated from the fitting. Figures 5(c) and (d) show the fwhm and the relative phase fractions (against rutile fraction) for CPC and IPC methods, respectively. The results suggest that the phase composition and the crystallinity for IPC method change with the deposition time. In comparison, the phase composition and crystallinity for CPC are relatively invariant.

Figure 6 shows the effects of the deposition time and the rotation speed on the OV and OC amounts from TGA-MS analysis for IPC and CPC. Digital photographs of the samples are also shown as a qualitative indicator of TiO_2 non-stoichiometry in which a blue coloration signifies the presence of oxygen vacancies [1, 18]. Here, IPC-300 rpm corresponds to the conditions used by Tolmachoff *et al.* [19]. It is noted that 40 l/min N_2 jets was used, compared to 100 l/min CDA jets used here. However, no deposition time was reported so no direct comparison is made here.

For a fixed deposition time (5 min), the effect of the rotation speed is shown in Fig. 6(a). The rotation speed mainly affects the convective cooling of the substrate [5, 19]. The deposition time is fixed at 5 min to minimise the oxidation from prolonged exposure to the flame. Surprisingly the OV amount only changes slightly with the rotation speed which is consistent with the sample colors. This suggests that the difference in the substrate temperature is not sufficient to oxidise the OVs for a short deposition time. This is due to the use of the cooling air jet to cool the plate in addition to the plate rotation. The high equivalence ratio of the flame also likely results in an oxygen-lean post-flame gas that minimises OV oxidation. On the other hand, the OC amount decreases as the rotation speed decreases as the more volatile components are likely to be burned.

The effect of the deposition time for IPC is summarised in Fig. 6(b). The rotation speed is fixed at 300 rpm while the deposition time is varied from 5 to 30 min. The OV and OC amounts are shown to drastically decrease with the deposition time. This also induces the color change to lighter blue. These results demonstrate the challenges of using the IPC method for applications that require a large volume of samples to be prepared. Specifically, in order to prepare the sample with a high amount of OV, a short deposition time is required which only produces a very small amount of sample [23]. In such a case, a large number of experiments have to be performed which could become impractical. Further, due to the continuous exposure of the sample to the flame, the sample prepared with a long deposition time (30 min) is essentially a mixture of freshly deposited samples with a high OV concentration and samples deposited earlier, *i.e.* non-homogeneous.

Compared to IPC, the continuous collection approach (CPC) effectively acts as a flow reactor. Figure 6(d) shows the OV and OC amounts are invariant to the deposition time, indicating that the system reaches a steady state in this condition. This is consistent with
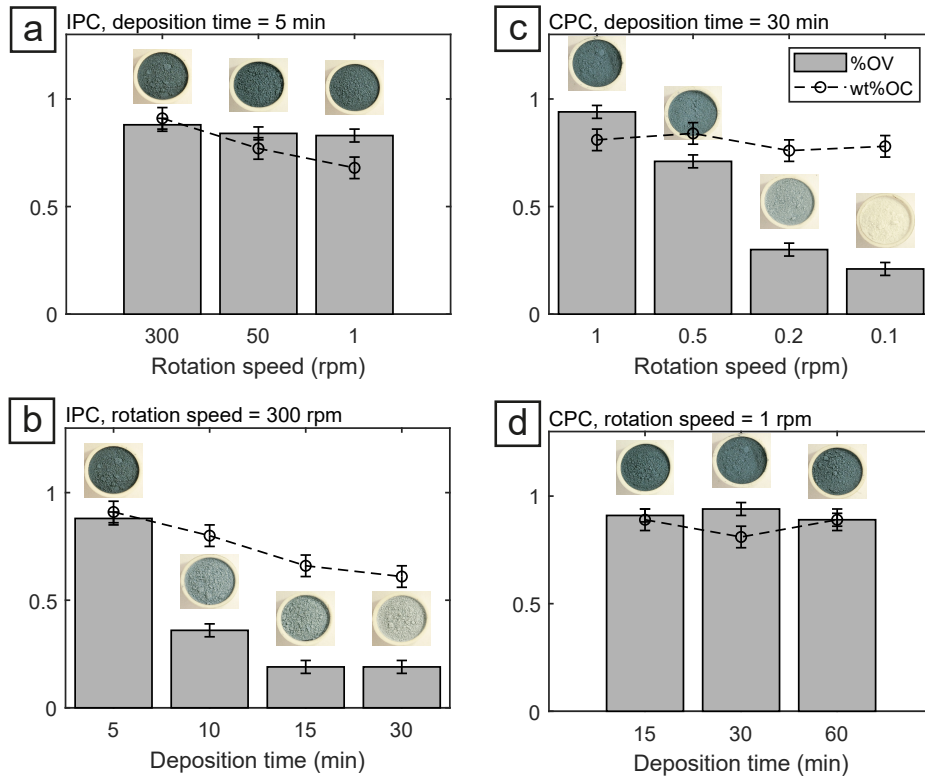
Figure 6: *The amounts of oxygen vacancy and organic component as functions of (a,c) the rotation speed and (b,d) the deposition time for the interval particle collection (IPC) and the continuous particle collection (CPC) approaches. The digital photographs of the samples are included to show the color changes.*

the measured phase composition and crystallinity in Fig. 5(c). This overcomes the problematic properties-yield correlation inherent in the IPC method. It is also noted that the OV and OC amounts are similar to IPC-300rpm-5min, suggesting that minimal OV oxidation occurs with CPC-1rpm conditions despite the significantly lower rotation speed.

As the rotation speed is reduced in CPC, a higher plate temperature and a longer exposure of deposited particles to the flame are expected. These factors result in a higher degree of oxidation of the OVs. Figure 6(c) shows that the OV amount and the blue coloration decrease with decreasing rotation speed. On the other hand, the higher plate temperature is expected to result in more carbon oxidation while the longer exposure time favours carbon deposition. Hence, the OC amount remains relatively constant.

4 Conclusions

Two different particle collection approaches in an FSRS reactor are investigated. The interval particle collection (IPC), the typical approach used in the literature, is effectively a batch reactor. On the other hand, a simple modification allows the reactor to be operated

continuously as a flow reactor, termed the continuous particle collection approach (CPC). The rotation speed and the deposition time are two important collection parameters assessed for both IPC and CPC.

For a short deposition time, IPC is found to produce a high OV amount regardless of the rotation speed. However, as the deposition time increases, the particle properties including the phase composition, crystallinity, OV and OC amounts change significantly. This means that the synthesis yield is correlated with particle properties which could be problematic for applications requiring a large volume of samples. On the other hand, the particle properties are found to be relatively unchanged with the deposition time for CPC. This allows the synthesis to be run for a longer time without compromising the properties of the prepared samples. In this case, the high OV amount could still be maintained or tuned for specific applications by controlling the rotation speed.

The findings in this paper introduce a strategy to increase the throughput of the flame synthesis using a divergence stabilised stagnation flame (DSSF), or specifically a flame stabilised on a rotating surface (FSRS) configuration. This opens up the potential use of flame-made materials for applications such as catalysis which will be explored in future works.

Acknowledgements

A Appendices

A.1 Plate temperature measurements

Plate temperature measurements were done with K-type sheathed thermocouple wires (Omega, TJC36-CASS-020U-6) placed in contact with the top surface of the rotating plate for selected flame conditions. The contact points are illustrated in Fig. 7. No precursor is used as particle deposition on the thermocouples will impact the reading. The average plate temperatures at the different points on the plate are summarised in Table 1. At higher rotation speeds, friction between the thermocouples and the plate may result in artificially elevated temperatures. At point 1, closest to the flame, the thermocouple is also directly heated by the hot gas from the flames so the readings may not reflect the actual plate temperature.
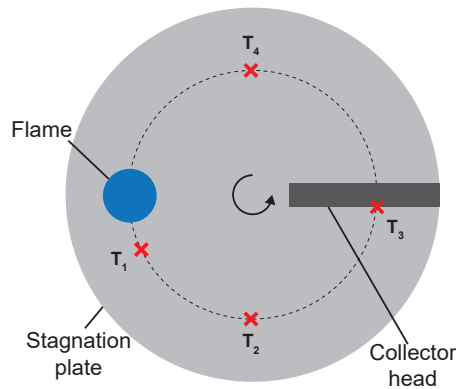
Figure 7: *A schematic of measurement locations (top-down view).*

Table 1: *Measured average plate temperatures.*

Flame conditions ER, rot. speed	T_1 (°C)	T_2 (°C)	T_3 (°C)	T_4 (°C)
ER = 1.2, 300 rpm	504	166	128	122
ER = 1.2, 100 rpm	388	153	129	139
ER = 1.2, 1 rpm	363	153	108	121
ER = 1.1, 1 rpm	320	151	109	119
ER = 1.05, 1 rpm	309	143	105	115
ER = 1.0, 1 rpm	295	137	102	111
ER = 0.9, 1 rpm	241	131	92	101

A.2 Powder XRD fitting

The measured powder XRD data for all samples are shown in Fig. 8.

Figure 8: *Measured powder XRD data for all samples discussed in this manuscript.*

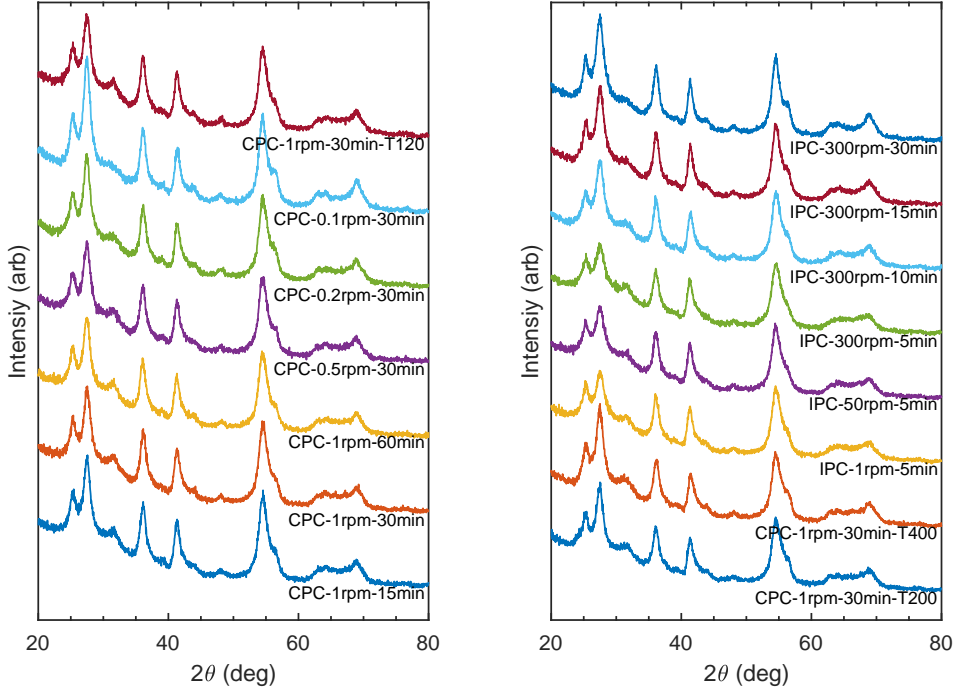A simple peak fitting exercise was performed to deconvolute quantitative phase information from the powder XRD data using TOPAS-Academic (ver. 6). A full profile fitting was not successful due to the significant overlaps and broadening of peaks from rutile, anatase and TiO_2-II phases.

The 2θ range of 15–34° was chosen as this range contains the strongest peaks from all phases with minimal overlap. Five peaks that are present in this range are A(101), II(110), R(110), II(111), and II(020), at 25.42°, 25.47°, 27.45°, 31.42°, and 32.56°, respectively (Anatase ICSD 92363, Rutile ICSD 16636, TiO_2-II ICSD 158778). However, only 3 peaks are used to fit the XRD data as A(101) and II(110) peaks are nearly coincidental, as well as II(111) and II(020) peaks. These peaks are referred to as peak 1–3 and fitted with Lorentzian functions with freely refinable centroid ($x_\circ$), intensity (I), and full width at half maximum (fwhm).

The background is modelled with a combination of a first order Chebyshev polynomial function and a $1/x$ function with a total of 3 refinable parameters, c_0, c_1, and c_2, i.e.

$$\text{Bkg}_i = \sum_{k=0}^{1} c_k T_k(x_i) + \frac{c_2}{2\theta_i} \tag{A.1}$$

Additionally, a broad Gaussian peak is added to represent the amorphous phase with freely refinable parameters I_{am} and $fwhm_{am}$ but the centroid (x_{am}) constrained to be the same for all data sets. The refined parameters are summarised in Table 2 while the plots are shown in Fig. 9.

The intensities of the fitted peaks can be written as the contribution of the individual peaks,

$$I_1 = I_{A(101)} + I_{II(110)} \tag{A.2}$$

$$I_2 = I_{R(110)} \tag{A.3}$$

$$I_3 = I_{II(111)} + I_{II(020)}. \tag{A.4}$$

The intensity ratio $(I_{II(111)} + I_{II(020)})/I_{II(110)} = 2.973$, calculated from the structure factor, accounting for the multiplicities, the Lorentz factor, and the polarization. The phase fractions, including amorphous phase, is assumed to be proportional to the intensities of their main peaks,

$$f_A \propto I_{A(101)} = I_1 - \frac{I_3}{2.973} \tag{A.5}$$

$$f_R \propto I_{R(110)} = I_2 \tag{A.6}$$

$$f_{II} \propto I_{II(111)} + I_{II(020)} = I_3 \tag{A.7}$$

$$f_{am} \propto I_{am}. \tag{A.8}$$

Subsequently, the relative fractions of the phases relative to rutile's are given by

$$f_A/f_R \propto \frac{I_1}{I_2} - \frac{I_3}{2.973 I_2} \tag{A.9}$$

$$f_{II}/f_R \propto \frac{I_3}{I_2} \tag{A.10}$$

$$f_{am}/f_R \propto \frac{I_{am}}{I_2}. \tag{A.11}$$

The relative fractions are shown in Fig. 10 and used to assess the effects of the operating conditions on the phase composition. Additionally, the fitted fwhms for peaks 1–3 are plotted as an indicator for crystallinity.

Table 2: *Fitted parameters for XRD data with $2\theta = 15 - 34°$ range. The parameters are given in 2θ (°) where applicable. All parameters are refined freely except for the centroid of amorphous Gaussian peak (x_{am}), which is constrained to be the same for all sets.*

Sample	x_1	I_1	fwhm$_1$	x_2	I_2	fwhm$_2$	x_3	I_3	fwhm$_3$
CPC-1rpm-15min	25.33	1227	1.25	27.49	2481	1.21	31.61	414	1.38
CPC-1rpm-30min	25.33	1133	1.17	27.53	2432	1.25	31.61	449	1.36
CPC-1rpm-60min	25.28	1074	1.13	27.46	2364	1.21	31.54	534	1.51
CPC-0.5rpm-30min	25.27	1066	1.16	27.48	2345	1.24	31.60	467	1.62
CPC-0.2rpm-30min	25.26	1293	1.25	27.47	2705	1.25	31.62	402	1.76
CPC-0.1rpm-30min	25.30	1463	1.11	27.47	3936	1.29	31.15	800	3.05
CPC-1rpm-30min-TGA120	25.28	1149	1.21	27.49	2502	1.26	31.55	499	1.36
CPC-1rpm-30min-TGA200	25.24	1364	1.42	27.47	2429	1.22	31.57	626	2.06
CPC-1rpm-30min-TGA400	25.33	1510	1.22	27.48	3601	1.42	31.38	1475	3.01
IPC-1rpm-5min	25.30	1140	1.21	27.54	2214	1.53	31.61	247	1.08
IPC-50rpm-5min	25.29	1070	1.30	27.50	2217	1.53	31.66	253	1.18
IPC-300rpm-5min	25.29	1087	1.42	27.53	2016	1.54	31.58	306	1.11
IPC-300rpm-10min	25.25	1237	1.38	27.50	3076	1.47	31.52	576	2.09
IPC-300rpm-15min	25.32	1187	1.09	27.52	3504	1.47	31.56	381	1.88
IPC-300rpm-30min	25.29	1144	1.01	27.48	4025	1.52	31.36	425	2.03

(continued)

| Sample	c_0	c_1	c_2	x_{am}	I_{am}	fwhm$_{am}$	gof
CPC-1rpm-15min	-448.6	-793.9	24985.5	33.99	26778	18.25	1.03
CPC-1rpm-30min	-586.1	-645.4	29199.7	33.99	25136	18.97	1.05
CPC-1rpm-60min	-614.6	-699.1	28759.3	33.99	26145	18.95	1.00
CPC-0.5rpm-30min	-817.6	-575.9	33394.1	33.99	25581	19.57	1.01
CPC-0.2rpm-30min	-286.0	-791.5	22741.6	33.99	22136	16.81	1.02
CPC-0.1rpm-30min	-274.9	-412.9	28772.2	33.99	9129	13.27	1.07
CPC-1rpm-30min-TGA120	-509.2	-628.7	28336.7	33.99	22905	18.40	1.04
CPC-1rpm-30min-TGA200	-328.0	-649.3	25745.1	33.99	18679	16.52	1.08
CPC-1rpm-30min-TGA400	-140.6	-567.9	24573.9	33.99	10997	13.70	1.03
IPC-1rpm-5min	-565.9	-799.9	26748.7	33.99	27959	17.98	1.04
IPC-50rpm-5min	-630.5	-929.0	25613.2	33.99	32058	18.20	1.02
IPC-300rpm-5min	-403.5	-911.2	22490.1	33.99	28913	17.93	1.02
IPC-300rpm-10min	-68.6	-766.1	20098.3	33.99	18340	15.61	1.05
IPC-300rpm-15min	-143.7	-884.8	19976.8	33.99	21845	15.87	1.00
IPC-300rpm-30min	-291.1	-434.4	28687.8	33.99	10839	14.27	1.04
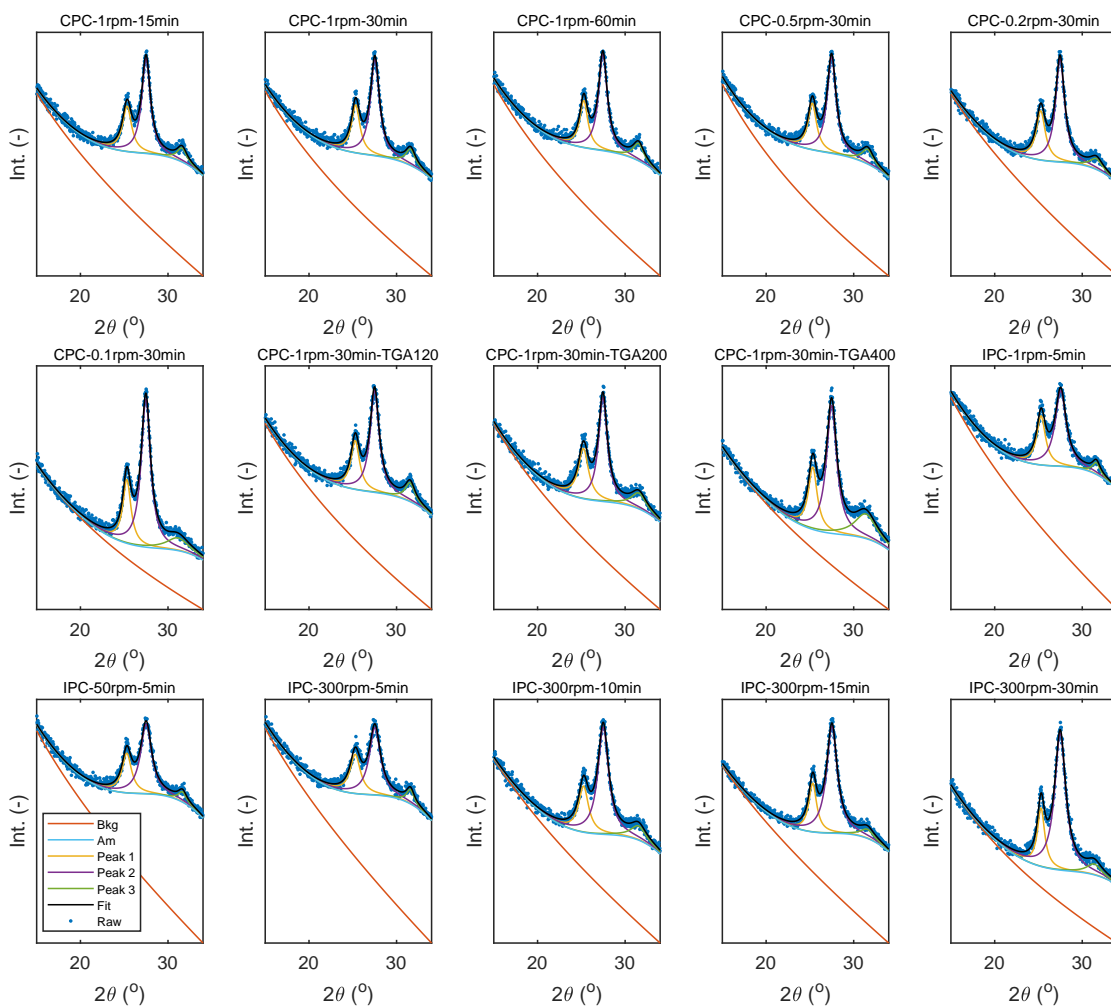
Figure 9: *Fitted XRD data for all dataset used in this work. Sample names are indicated on the plot title. The blue markers denote the experimental data while the lines represent the fitted profiles (black) and the individual components (other colours). The fitted parameters are summarised in Table 2.*

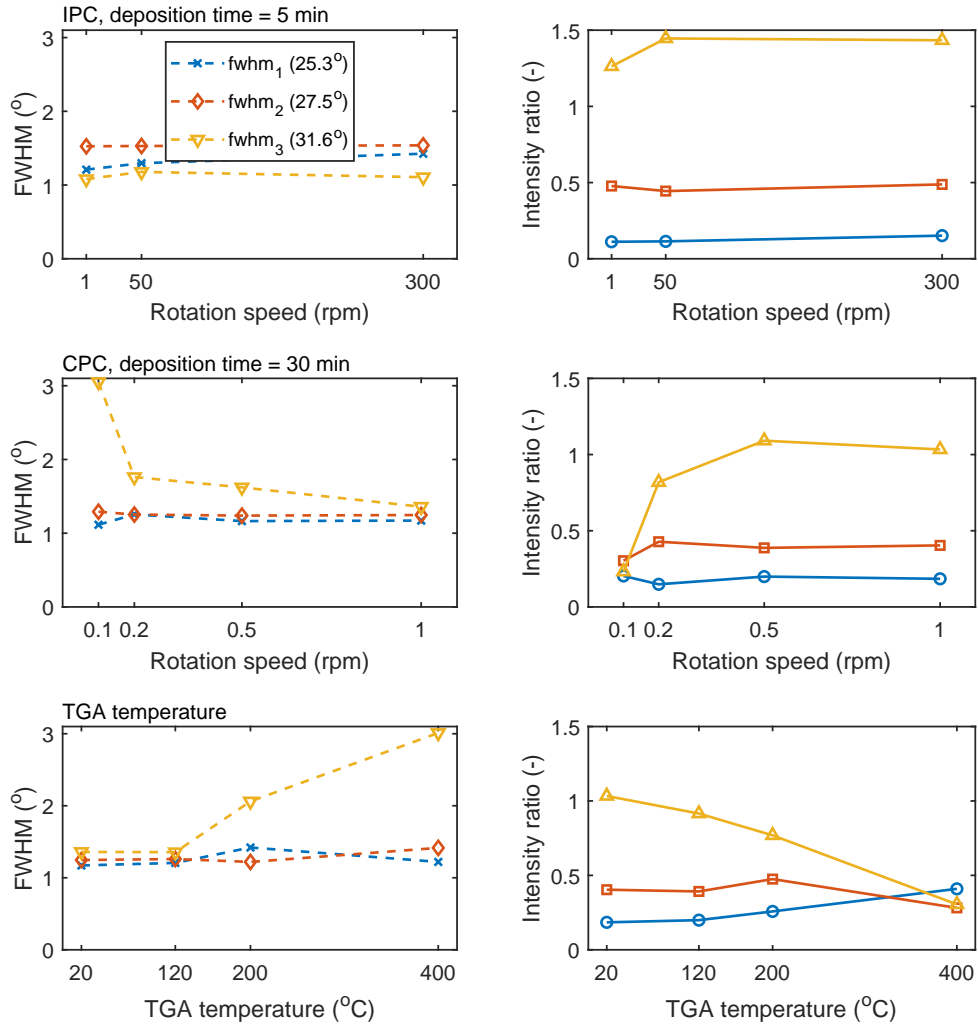**Figure 10:** *Full width at half maximum (fwhm) for peaks 1–3 (left), and the fractions of anatase, TiO$_2$-II, and amorphous phases relative to rutile fraction (right) for different collection conditions and TGA temperature (for CPC-1rpm-30min sample).*

A.3 TGA-MS analysis

The average normalised weights at different heating stages, MS signal ratios, and the derived weight changes due to carbon oxidation and oxygen vacancy oxidation are summarised in Table 3 for all samples discussed in this manuscript. A commercial TiO_2 (Sigma) sample is also analysed, showing oxygen vacancy content of $\sim 0\%$ while the OC content is $\sim 0.2\%$.

Table 3: *TGA-MS results and the estimated oxygen vacancy and organic component amounts for all samples discussed in this paper.*

Sample	w_{1B} (%)	w_{1C} (%)	w_{1D} (%)	w_{2B} (%)	w_{2C} (%)	w_{2D} (%)
P25	100.935	100.570	100.065	100.639	100.337	100
P25 (repeat)	100.888	100.532	100.051	100.626	100.334	100
IPC-1rpm-5min	101.766	101.323	99.966	101.451	100.800	100
IPC-50rpm-5min	101.860	101.394	99.929	101.499	100.819	100
IPC-300rpm-5min	101.919	101.447	99.894	101.468	100.809	100
IPC-300rpm-10min	102.134	101.494	99.925	101.548	100.868	100
IPC-300rpm-15min	102.040	101.383	99.967	101.488	100.827	100
IPC-300rpm-30min	101.965	101.289	99.949	101.485	100.821	100
CPC-1rpm-15min	101.974	101.534	99.955	101.492	100.821	100
CPC-1rpm-30min	101.955	101.514	99.970	101.547	100.849	100
CPC-1rpm-60min	102.083	101.598	99.982	101.566	100.855	100
CPC-0.5rpm-30min	102.067	101.560	99.966	101.545	100.854	100
CPC-0.2rpm-30min	102.148	101.489	99.967	101.544	100.852	100
CPC-0.1rpm-30min	102.204	101.519	99.950	101.561	100.862	100

(continued)

Sample	R (-)	Δw_C (%)	Δw_O (%)	OV (at%)
P25	0.42	0.24	0.01	0.02
P25 (repeat)	0.36	0.20	-0.01	-0.03
IPC-1rpm-5min	0.22	0.68	0.33	0.83
IPC-50rpm-5min	0.19	0.77	0.33	0.84
IPC-300rpm-5min	0.23	0.91	0.35	0.88
IPC-300rpm-10min	0.15	0.80	0.14	0.36
IPC-300rpm-15min	0.12	0.66	0.07	0.19
IPC-300rpm-30min	0.17	0.61	0.07	0.19
CPC-1rpm-15min	0.18	0.89	0.37	0.91
CPC-1rpm-30min	0.17	0.81	0.38	0.94
CPC-1rpm-60min	0.17	0.89	0.36	0.89
CPC-0.5rpm-30min	0.14	0.84	0.28	0.71
CPC-0.2rpm-30min	0.13	0.76	0.12	0.30
CPC-0.1rpm-30min	0.10	0.78	0.08	0.21

A.4 Particle size measurements

Particle size distributions were measured for selected samples by TEM image analysis. The results are shown in Fig. 11.
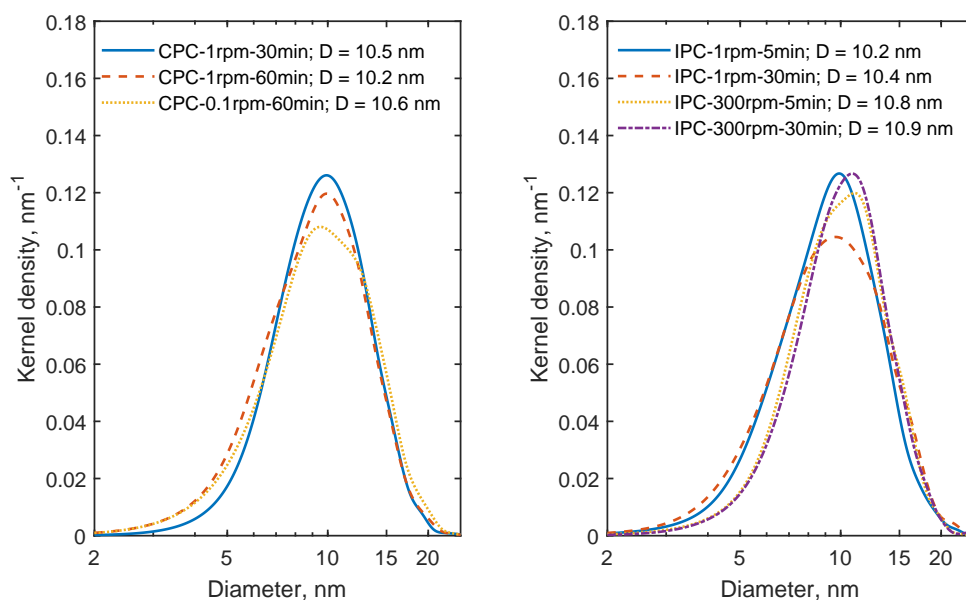

Figure 11: *Measured particle size distributions from TEM image analysis. The median particle sizes are denoted on the legend.*

References

[1] R. G. Breckenridge and W. R. Hosler. Electrical properties of titanium dioxide semi-conductors. *Phys. Rev.*, 91(4):793–802, 1953.

[2] E. J. Bringley, M. Y. Manuputty, C. S. Lindberg, G. C. Leon, J. Akroyd, and M. Kraft. Simulations of TiO_2 nanoparticles synthesised off-centreline in jet-wall stagnation flames. *J. Aerosol Sci.*, (Accepted for publication), 2021.

[3] A. A. Coelho. TOPAS and TOPAS-Academic: an optimization program integrating computer algebra and crystallographic objects written in C++. *J. Appl. Crystallogr.*, 51:210–218, 2018.

[4] Y. Gao, Y. Liang, and S. A. Chambers. Thermal stability and the role of oxygen vacancy defects in strong metal support interaction – Pt on Nb-doped $TiO_2(100)$. *Surf. Sci.*, 365(3):638–648, 1996.

[5] L. Hu, Z. Miao, Y. Zhang, H. Zhang, and H. Yang. Numerical assessment on rotation effect of the stagnation surface on nanoparticle deposition in flame synthesis. *Materials (Basel).*, 12(9), 2019.

[6] R. J. Kee, J. A. Miller, G. H. Evans, and G. Dixon-Lewis. A computational model of the structure and extinction of strained, opposed flow, premixed methane-air flames. *Proc. Combust. Inst.*, 22(1):1479–1494, 1989.

[7] L. Y. Lin, S. Kavadiya, X. He, W. N. Wang, B. B. Karakocak, Y. C. Lin, M. Y. Berezin, and P. Biswas. Engineering stable Pt nanoparticles and oxygen vacancies on defective TiO_2 via introducing strong electronic metal-support interaction for efficient CO_2 photoreduction. *Chem. Eng. J.*, 389:123450, 2020.

[8] C. Lindberg, M. Manuputty, P. Buerger, J. Akroyd, and M. Kraft. Numerical simulation and parametric sensitivity study of titanium dioxide particles synthesised in a stagnation flame. *J. Aerosol Sci.*, 138, 2019.

[9] C. Liu, J. Camacho, and H. Wang. Phase equilibrium of TiO_2 nanocrystals in flame-assisted chemical vapor deposition. *ChemPhysChem*, 19(2):180–186, 2018.

[10] M. Y. Manuputty, J. Akroyd, S. Mosbach, and M. Kraft. Modelling TiO_2 formation in a stagnation flame using method of moments with interpolative closure. *Combust. Flame*, 178:135–147, 2017.

[11] M. Y. Manuputty, J. A. H. Dreyer, Y. Sheng, E. J. Bringley, M. L. Botero, J. Akroyd, and M. Kraft. Polymorphism of nanocrystalline TiO_2 prepared in a stagnation flame: formation of the TiO_2-II phase. *Chem. Sci.*, 10:1342–1350, 2019.

[12] M. Y. Manuputty, C. S. Lindberg, M. L. Botero, J. Akroyd, and M. Kraft. Detailed characterisation of TiO_2 nano-aggregate morphology using TEM image analysis. *J. Aerosol Sci.*, 133:96–112, 2019.

[13] M. Y. Manuputty, C. S. Lindberg, J. A. H. Dreyer, J. Akroyd, J. Edwards, and M. Kraft. Understanding the anatase-rutile stability in flame-made TiO_2. *Combust. Flame*, 226:347–361, 2021.

[14] T. Mazza, E. Barborini, P. Piseri, P. Milani, D. Cattaneo, A. Li Bassi, C. E. Bottani, and C. Ducati. Raman spectroscopy characterization of TiO_2 rutile nanocrystals. *Phys. Rev. B*, 75(4), 2007.

[15] J. A. Miller and R. J. Kee. Chemical kinetics and combustion modeling. *Annu. Rev. Phys. Chem.*, 41:345–387, 1990.

[16] S. Mohajernia, P. Andryskova, G. Zoppellaro, S. Hejazi, S. Kment, R. Zboril, J. Schmidt, and P. Schmuki. Influence of Ti^{3+} defect-type on heterogeneous photocatalytic H_2 evolution activity of TiO_2. *J. Mater. Chem. A*, 8(3):1432–1442, 2020.

[17] R. Mueller, H. K. Kammler, K. Wegner, and S. E. Pratsinis. OH surface density of SiO_2 and TiO_2 by thermogravimetric analysis. *Langmuir*, 19(1):160–165, 2003.

[18] A. Teleki and S. E. Pratsinis. Blue nano titania made in diffusion flame. *Phys. Chem. Chem. Phys.*, 11(19):3742–3747, 2009.

[19] E. D. Tolmachoff, A. D. Abid, D. J. Phares, C. S. Campbell, and H. Wang. Synthesis of nano-phase TiO_2 crystalline films over premixed stagnation flames. *Proc. Combust. Inst.*, 32(2):1839–1845, 2009.

[20] E. D. Tolmachoff, S. Memarzadeh, and H. Wang. Nanoporous titania gas sensing films prepared in a premixed stagnation flame. *J. Phys. Chem. C*, 115(44):21620–21628, 2011.

[21] H. Wang, D. J. Phares, and E. D. Tolmachoff. Method for prepraring metal oxide crystalline nanoparticle films for dye sensitized solar cell photoanodes. *U.S. Patent No.*, 8,329,251 B2, 2012.

[22] S. Wu, W. Wang, W. Tu, S. Yin, Y. Sheng, M. Y. Manuputty, M. Kraft, and R. Xu. Premixed stagnation flame synthesized TiO_2 nanoparticles with mixed phases for efficient photocatalytic hydrogen generation. *ACS Sustain. Chem. Eng.*, 6(11):14470–14479, 2018.

[23] S. Wu, M. Y. Manuputty, Y. Sheng, H. Wang, Y. Yan, M. Kraft, and R. Xu. Flame synthesized blue TiO_{2-x} with tunable oxygen vacancies from surface to grain boundary to bulk. *Small Methods*, 2000928, 2020.